Semi-solid constitutive parameters and failure behavior of a cast AA7050 alloy

T Subroto[1,2,3*], D G Eskin[3,4], A Miroux[1,2,5], K Ellingsen[6], M M'Hamdi[6,7,8], L Katgerman[2]

[1] Materials innovation institute (M2i), Mekelweg 2, Delft, 2628 CD, The Netherlands

[2] Department of Materials Science and Engineering, Delft University of Technology, Mekelweg 2, Delft, 2628 CD, The Netherlands

[3] BCAST, Brunel University, Uxbridge, Middlesex, UB8 3PH, United Kingdom

[4] Tomsk State University, Tomsk, 634050, Russia

[5] Aleris Aluminium Duffel, 2570 Duffel, Belgium

[6] SINTEF Materials and Chemistry, NO-0314 Oslo, Norway

[7] SINTEF Materials and Chemistry, NO-7465 Trondheim, Norway

[8] Department of Materials Science and Engineering, Norwegian University of Science and Technology, N-7491 Trondheim, Norway

*) corresponding author, e-mail: Tungky.subroto@gmail.com, Tungky.subroto@brunel.ac.uk

Abstract

AA7050 is an aluminum alloy with superior mechanical properties, however it is prone to hot tearing (HT) during its production via direct-chill casting. This study focuses on extracting constitutive parameters of the alloy thermomechanical behaviour in semi-solid state, as well as gaining insight in its failure behavior. Tensile tests were performed using an Instron 5944 at solid fractions between 0.85 (550 °C) and 1.0 (465 °C), at deformation rates of 0.2 and 2 mm/min. The results showed that there are three mechanical behavior regimes in this solid fraction range; ductile at 1.0 (T = 465 °C) ≤ f_s < 0.97 (T = 473 °C), brittle at 0.97 (T = 473 °C) ≤ f_s ≤ 0.9 (T = 485 °C), and then ductile again (at 0.9 (T = 485 °C) < f_s ≤ 0.85 (T = 550 °C)). Fracture surface analysis revealed that the fracture mode was mostly intergranular with fracture propagating through solid bridges as well. Semi-solid constitutive parameters were obtained by making a simple thermal model and numerical tensile tests in ALSIM software package and comparing the simulation results with experimental mechanical tests. The extracted constitutive parameters and available information from the literature supports the fact that AA7050 is more susceptible to HT as compared to AA5182 and Al-2%Cu alloys. The obtained parameters can further enhance the predictive capability of computer simulations of direct-chill casting.

Keywords: Semi-solid mechanical properties, numerical simulation, thermal modelling, constitutive parameters, fracture surface analysis, hot tearing

1. Introduction

AA7XXX-series aluminum alloys are critical for structural applications in aerospace industries due to their superior mechanical properties, such as high strength and enhanced fracture toughness [1,2]. One major route to produce this type of alloys for further downstream processing is through direct-chill casting (DC casting) [3].

42 Although DC casting is a robust production method and able to meet industrial standards, the nature
43 of the process introduces severe thermal gradients in a cast ingot during casting. The shell of the ingot
44 that has just solidified comes in direct contact with cooling water, while the centre of the ingot is still
45 partially liquid or, in larger ingots, may be still in the fully liquid state. These thermal gradients in
46 connection with greatly different mechanical behaviour of the different sections of the ingot augment
47 the formation of casting defects, in particular hot tear (HT) and cold crack (CC).

48 HT is one of the critical solidification defects that may form during casting. It occurs when the alloy is
49 at its semi-solid state, especially towards the end of solidification (below the rigidity temperature
50 when the dendrites have connected to each other and the alloy has gained some mechanical strength)
51 where there is no sufficient melt to feed the shrinkage, which under imposed thermal stresses may
52 result in crack formation in the billet. HT has different levels of severity, starting from micro-scale HT
53 which can be healed through further processing, i.e. hot-isostatic-pressing[4], up to the catastrophic
54 level where the solidified billet cannot be used for subsequent processing and rendered useless. In
55 any case, the presence of HT in the billet will reduce the quality of the cast product and increase the
56 production cost of the alloy, thus needs to be minimized.

57 HT formation has been extensively studied and reviewed, see Ref. [5] for the conditions and
58 mechanisms of HT formation and Ref. [6] for the properties of semi-solid alloys, which are directly
59 linked to the HT phenomenon. Susceptibility of the alloy to HT depends on both microscopic and
60 macroscopic features of the alloy. Grain size (including secondary dendrite arms spacing) [7] and the
61 presence of harmful intermetallics in the structure [8] may affect the HT susceptibility. Meanwhile, the
62 chemical composition [9] affects the semi-solid mechanical behavior of the alloy [6,10–12] through the
63 phase composition but also through the freezing range of the alloy [6,9] – the wider, the more
64 susceptible to HT. However, it is also understood that the longer the portion of solidification part
65 where melt feeding is insufficient as compared to the part of the solidification range where feeding is
66 still active, the more the alloy is prone to HT [13]. The uneven cooling conditions in the ingot due to
67 the nature of the DC casting process result in tensile thermal stresses imposed on the part of the billet
68 which is still in the semi-solid state. This, combined with insufficient melt feeding to the formed
69 dendritic network, may lead to the formation of HT [11,12]. Therefore, to better understand the HT
70 susceptibility of an alloy, it is crucial to take into account the onset thermal contraction temperature
71 (determining the beginning of the temperature range vulnerable to HT) as well as the total amount of
72 thermal contraction (correlated to the strain imposed on the semi-solid material). An AA7050 alloy
73 has a relatively long freezing range [14] and the thermal contraction starts at a relatively low solid
74 fraction as compared to other alloys [15–17]. Combined with DC casting conditions that aggravate the
75 thermomechanical condition in the solidifying ingot, it can be inferred that producing a quality AA7050
76 billet through DC casting is difficult due to its propensity to HT occurrence. Additionally, an AA7050
77 alloy demonstrates large thermal expansion and low thermal conductivity, which implies that large
78 thermal residual stress could be generated during cooling, and ultimately makes this alloy prone to
79 CC. Since catastrophic CC may be initiated through micro-scale HT acting as pre-existing cracks [18], the
80 formation of HT is intimately related to CC. A careful selection of process conditions to produce sound
81 AA7050 billets without HT and CC needs to be done. This is because CC not only reduces the
82 productivity of a manufacturing company but also poses safety hazard for the casting personnel and
83 hardware, thus needs to be minimized.

84 For decades, the R&D efforts were focused on minimizing the HT occurrence during DC casting
85 (without changing the alloy compositions). Those included finding the best casting temperature [19]
86 and trying various melt flow schemes to feed the liquid pool [20]. It was also clear that reducing the
87 casting speed was the most effective way to reduce HT [9]. However, reducing casting speed implies

88 lowering the production rate, and hence the profitability of the company. Thus, an optimum casting
89 speed has to be found to maximize the casting performance and quality. Traditionally, this is done by
90 trial and error. However, with the advent of powerful computers, numerical process optimization is
91 the preferable course of action as it saves both time and resources.

92 In this work, we used ALSIM, a numerical model enabling us to simulate aluminum casting processes.
93 This package includes an advanced solidification model which accounts for solidification defects such
94 as HT and CC [21,22]. In order to simulate the casting process accurately, this model needs a set of
95 constitutive parameters which are unique for different alloys. Such parameters are typically obtained
96 by fitting a set of model parameters to the experimental data. At the moment, ALSIM only has
97 constitutive parameters for an AA7050 alloy in the fully solid state [23], and in the sub-solidus regime[24].
98 Hence, ALSIM is currently lacking constitutive behavior database for the semi-solid regime of an
99 AA7050 alloy [20], needed for modelling HT behavior. Instead, the Al-2% Cu data is used to complete
100 the semi-solid part of the database. However, thermophysical properties of these two alloys are
101 different (e.g. freezing range of AA7050 is 170 °C while that of Al-2% Cu is 107 °C). This gap in the
102 AA7050 database is critical because the semi-solid part of the database is directly linked to the HT
103 susceptibility of the alloy, thus needs to be completed.

104 The goal of this work was twofold. Firstly, we aimed at completing the ALSIM thermomechanical
105 database in the semi-solid temperature region of an AA7050 alloy. The experimental data required by
106 ALSIM to fit the model includes the constitutive tensile mechanical behavior in the semi-solid
107 temperature range, which can be obtained through isothermal tensile tests. The solid fraction range
108 of interest is below the solid fraction (f_s) ~ 0.8 [15] (the temperature when mechanical properties of the
109 alloy start to be appreciated, typically described as a rigidity point [25]) down to the nonequilibrium
110 solidus. The tensile mechanical behavior is critical as it is the main mode for HT to happen (the force
111 imposed onto the central part of a bilet is in outward radial direction due to the cooling direction in
112 DC casting). Constitutive parameters for the semi-solid ALSIM model were extracted by fitting the
113 model to the obtained experimental tensile curves. The constitutive parameters were obtained by
114 comparing the tensile force-displacement curves from the experimental tensile tests with the results
115 from numerical thermo-mechanical tensile tests that were built using ALSIM. Using this method, we
116 selected the constitutive parameters that provided us with a minimum difference between the
117 numerical and experimental tensile tests.

118 Secondly, we aimed at gaining insight in the mechanical behavior of the semi-solid alloy, which was
119 ultimately related to its HT susceptibility. The mechanical behavior of the alloy in the super-solidus
120 regime was quantified through the strength and its ability to accommodate deformation (ductility
121 characteristics) at different solid fractions. Additionally, we were also able to estimate the solid
122 fraction where the grain coalescence occurred – suggested by Giraud [26] as the transition point from
123 where the mechanical properties were governed by liquid films into state where mechanical
124 properties were controlled by solid bridges. At this point the material gains significant strength, thus
125 behaving more like a solid sample tested at a high temperature (i.e. higher strength and able to
126 accommodate more deformation). This transition point is important as it could be considered as the
127 stage where no continuous liquid film remains between the grain boundaries and the alloy is
128 sufficiently ductile to resist the HT formation[21], therefore it is an important variable to assess the
129 alloy susceptibility to HT. We also tested the alloy at two different pulling speeds to understand its
130 strain-rate sensitivity. Subsequently, failure mechanism of the tested samples at different solid
131 fractions was elucidated through fracture surface analysis in a scanning electron microscope (SEM). It
132 was reported that in the semi-solid regime there are different mechanical regimes (i.e. brittle and
133 ductile) [6], hence, it was important to examine this phenomenon in our AA7050 alloy. Furthermore,

134 we also discuss the HT propensity of an AA7050 alloy and compare it to other types of aluminum
135 alloys, in order to gain insight in its HT susceptibility based on the tensile mechanical properties and
136 other thermo-physical properties (i.e. the freezing range and the onset temperature of thermal
137 contraction).

138 The outcome from this work provides the research community not only with a database which enables
139 better accuracy of ALSIM to simulate DC casting of an AA7050 alloy, but also with insights in the HT
140 susceptibility of this alloy as compared to other types of aluminum alloys. This information will
141 ultimately be vital for optimization of AA7050 production.

142

143 **2. Materials and methods**

144 **2. 1. Experiments**

145 An AA7050 alloy used in this experiment was produced using direct-chill (DC) casting method and
146 supplied by Tata Steel Nederland Technology B.V. (IJmuiden). The melt was degassed in the furnace
147 and a conventional bore mold was utilized during DC casting. The produced billet had a diameter of
148 315 mm. Optical spectrum analysis was used to determine the chemical composition of the billet (see
149 Table I). The solidification path was simulated through JMAT Pro software shown in Figure 1.

Table I Average chemical composition of AA7050.

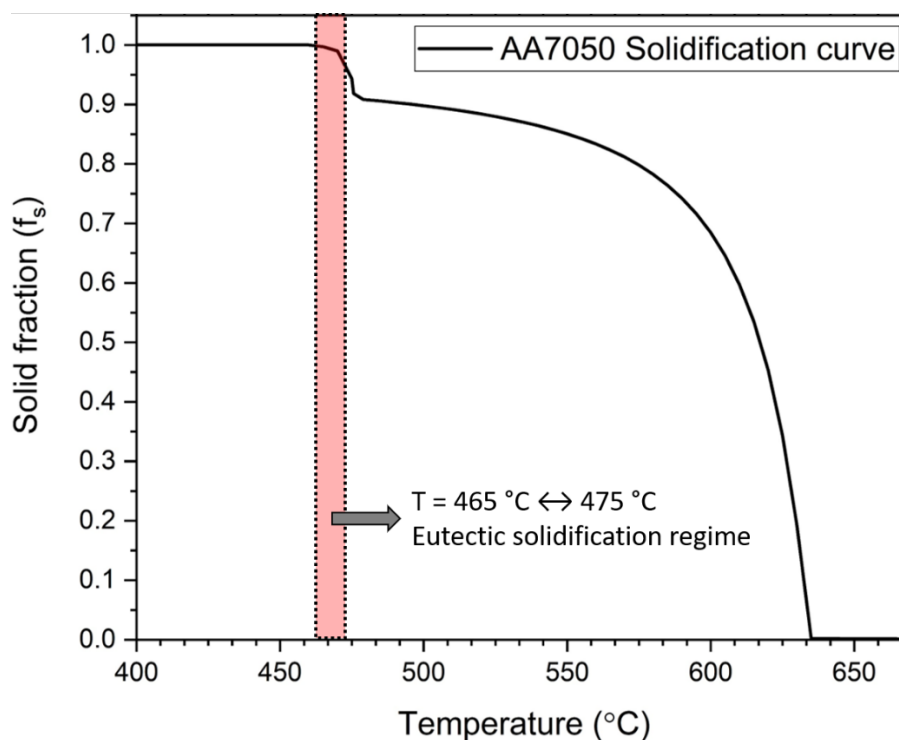| Elements, wt. pct.								
Zn	Cu	Mg	Zr	Fe	Mn	Si	Ti	Cr
6.15	2.2	2.1	0.13	0.07	0.04	0.04	0.03	< 0.01

150

Figure 1 Solidification path of AA7050 based on JMAT pro calculation

151

152　The tensile specimens were cut from the same billet from around mid-radius section parallel the
153　casting direction without any heat treatment. This assured that the samples had the same chemical
154　composition, not affected by macrosegregation. The specimens were tested using a set-up developed
155　at SINTEF Materials and Chemistry with an Instron 5944 series tensile test machine equipped with a
156　2-kN load cell. The specimen was heated up using an induction heating coil system. The temperature
157　in the center of the specimen was controlled by a calibrated thermocouple connected to a
158　Eurotherm™ temperature controller, which has temperature uncertainty is approximately ±0.35 °C
159　from the target temperature. The temperatures were measured using thermocouples calibrated
160　against the standard calibrated thermocouple and the primary values were corrected to the calibrated
161　values so that the estimated uncertainty in the temperature measurements did not exceed 0.8 °C. The
162　thermocouple was positioned in the central mid-length position of the sample, drilled from the edge
163　of the sample in the axial direction of the sample (see Fig. 2a) and the thermocouple was kept in place
164　by gravity force because we do not want to put extra force onto the semi-solid regime . The schematic
165　of the tensile test setup is shown in Figure 2a and the geometry of the tensile specimen is shown in
166　Figure 2b. The notch near the end of the specimen is designed to reduce the heat flow out of the
167　specimen by the water-cooled surface, thus flattening the temperature gradient across the specimen.

168　A boron-nitride coated quartz-glass tube (coating was only on the inside) was used to enclose the mid-
169　length part of the sample to prevent liquid breakout during the fully liquid phase. The coating was
170　intended to prevent the sticking of the liquid aluminum onto the quartz tube which may affect the
171　force measurement due to the additional friction resistance. The experimental cycle (for both heating
172　and mechanical testing temperature) is shown in Figure 2c.

173　The sample was first heated from room temperature up to T_{max} = 635 °C, which is just above the
174　liquidus of the AA7050 (Figure 1). After that, the samples were held at T_{max} for 60 s to ensure that the
175　central mid-length part of the specimen was fully liquid. Then we cooled down the sample to the test
176　temperature at a cooling rate of 1 °C/s. Subsequently, the sample was kept at the test temperature
177　for approximately 90 s to let the temperature across the specimen stabilize. Afterwards, the
178　mechanical deformation was performed with a specified displacement (pulling) rate until the force
179　value was approximately zero after the fracture. The accuracy and displacement resolution of the test
180　was 0.003 mm/s (0.2 mm/min).

181　Two different displacement rates was used (Table II); 0.2 mm/min was chosen to be the lowest
182　displacement-rate because at lower rates the liquid parts of the alloy start to stick to the quartz tube
183　and may increase the friction force, thus possibly the measurement error. To study the displacement-
184　rate sensitivity of the alloy at this temperature regime, pulling speed with an order of magnitude
185　higher (2 mm/min) was selected.

186

187

(a)

1. Water-cooled jaws
2. Tensile specimen (ø = 11.68 mm)
3. Quartz tube
4. Induction coil (for heating)
5. Thermocouple

All units are in millimeter (mm)

(b)

Steps:
(1) Heating/remelting
(2) Holding
(3) Cooling to test temperature
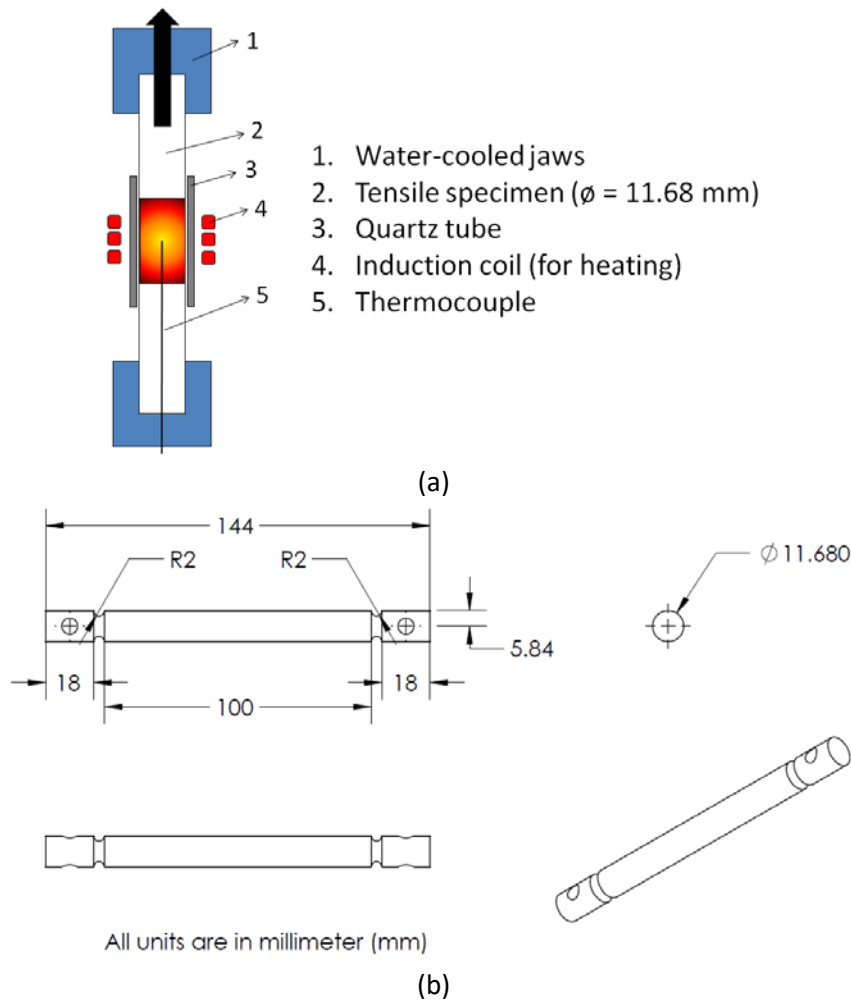(4) Stabilizing temperature
(5) Tensile testing

(c)

Figure 2. (a) Tensile test setup schematics, (b) tensile sample geometry, and (c) isothermal tensile test cycle; heating cycle (red line) and mechanical deformation cycle (blue line).

188   The test temperatures that we cover in this work correspond to the solid fractions (f_s) in the range
189   where HT typically occurs, i.e. between 0.85 (T = 550 °C), below rigidity temperature – where alloy
190   starts to gain mechanical strength, and 1.0 (T = 465 °C), when alloy is at fully solid state. We carried
191   out tensile tests at different data points, namely at different solid fractions (temperature) and
192   displacement-rate as shown in Table II. The solid fraction was correlated with the temperature based
193   on JMat-Pro® calculation depicted in Figure 1. Three tests were performed to obtain statistical

6

194 behavior of the alloy for each combination of temperature and displacement rate. In this work we
195 focus on tensile tests in a low strain-rate regime (i.e. between 10^{-3} and 10^{-5} s^{-1}), which is relevant to
196 DC casting [27]. Tests at a higher strain rate (2 mm/min) were only performed at specific temperature
197 points, which is approximately before and after typical grain coalescence point in different alloys
198 [26,28,29], to observe strain-rate sensitivity at different mechanical property regions. Tensile tests were
199 performed until each sample failed. Fracture surface analysis of the failed samples were carried out in
200 a Jeol JSM-6500F scanning electron microscope (SEM).

201

Table II Tensile plan matrix and the number of the test performed at different test conditions.

Test. Temp. (°C) / Disp. rate (mm/min)	465 (f_s=1.0)	470 (f_s = 0.99)	473 (f_s = 0.97)	475 (f_s = 0.94)	485 (f_s = 0.90)	520 (f_s = 0.88)	550 (f_s = 0.85)
0.2 mm/min	3	3	3	3	3	3	3
2.0 mm/min	0	3	0	3	3	0	0

202

2.2 ALSIM constitutive equations

204 Mechanical properties of alloys are different at different temperature ranges. There is a dramatic
205 change in the constitutive behavior of alloys in the vicinity of the solidus temperature due to the
206 significant change in morphology (spatial distribution of the remaining liquid phase), strength and
207 ductility of the alloy [26,30]. The semi-solid mechanical behavior of the alloy in ALSIM is described using
208 an advanced viscoplastic constitutive model to represent the coherent part of the semi-solid regime,
209 which allows for the dilatation/densification of the semisolid skeleton under applied deformation.
210 While the full account and detailed explanations of the model could be found elsewhere [28,31–34], for
211 brevity, in this work we are only focusing on the part of the model that deals with partial cohesion of
212 the mush as shown by Equations (1) and (2). The functions $\alpha(g_s, X)$ and $C^*(g_s, X)$ describe the evolution
213 of the partial cohesion of the mush and must be determined from careful rheological experiments at
214 various fractions of solids and stress states. For grain-refined Al-Cu alloys, Ludwig et al. [28] have shown
215 that the following expressions provide a simplified good fit with experimental data. For all stress states
216 (all X values) both functions are described as follows [14,21,28,29]:

$$C^*(g_s, X) = C^*(g_s, X = 0) + \frac{1 - C^*(g_s, X = 0)}{1 + \exp\left[\dfrac{X_0 - X}{\Delta x}\right]}$$

(1)

$$\alpha(g_s, X) = \alpha(g_s, X = 0)$$

(2)

219 Where:

$$C^*(g_s, X=0) = \frac{1-(1-g_s)^p}{1+\exp\left(\dfrac{g_s^{coh}-g_s}{\Delta g_s}\right)}$$

220
(3)

$$\alpha(g_s, X=0) = \frac{\alpha_0 + \alpha_1 \dfrac{g_s^{1/3}}{1-g_s^{1/3}}}{1+\exp\left(\dfrac{g_s^{coh}-g_s}{\Delta g_s}\right)}$$

221
(4)

222 In addition to the $\alpha(g_s, X)$ value for general stress states ($X = 0$), the most recent version of the model
223 [28,29] includes option to take into account the effect of coalescence in the tensile stress state – which
224 is the main mode of HT in DC casting, ($X < 0$) through $\alpha(g_s, X)$. The function is described as follows:

$$\alpha(g_s, X<0) = \frac{\alpha_0 + \alpha_1 \dfrac{g_s}{1-g_s}\exp(k(g_s - g_s^{coal}))}{1+\exp\left(\dfrac{g_s^{coh}-g_s}{\Delta g_s}\right)}$$

225
(5)

226 Where $k = 10$ and $g_s^{coal} = 0.94$ [18]. When the alloy becomes fully cohesive and reaches the fully solid
227 state (at $g_s = 1$, $C = 1$), the alloy becomes ductile and follows the creep law behavior. Therefore, the
228 viscoplastic strain-rate tensor could be simplified as follows [21,29]:

$$\dot{\boldsymbol{\varepsilon}}_s^p = \frac{3}{2}\frac{\dot{\varepsilon}_s^p}{\overline{\sigma}_s}\boldsymbol{\tau}_s$$

229
(6)

230 with

$$\overline{\sigma}_s = \sigma_0 \exp\left(\frac{Q}{nRT}\right)\left(\frac{\dot{\varepsilon}_s^p}{\dot{\varepsilon}_0}\right)^{1/n}$$

231
(7)

232 This law governs the behavior of the alloy until the merge properties temperature (T_{merge}) which is
233 usually a in the vicinity of solidus temperature (could be up to around 50 °C below solidus). From this
234 point down to onset hardening temperature (T_0) the alloy is governed by extended-Ludwik equation
235 or ALSPEN model (Eq. 8) [35]. However, since the hardening effect in this temperature range is not
236 significant, the hardening parameter ($r(T)$) is set to zero. Below T_0, the strain hardening of the alloy
237 starts to become important thus, $r(T)$ is non-zero. The formulation of full extended-Ludwik equation
238 used to simulate the mechanical behavior of the alloy at fully solid state is as follows:

$$\sigma = K(T)(\varepsilon_p + \varepsilon_p^0)^{r(T)}(\dot{\varepsilon}_p)^{m(T)}$$

239
(8)

240 Where $K(T)$ is the consistency of the alloy (at $\varepsilon = 1$, $\dot{\varepsilon} = 1$ s^{-1}), $r(T)$ is the hardening parameter and $m(T)$
241 is the strain-rate sensitivity of the alloy and the value is inversely proportional to n in eq. 7. These
242 parameters are temperature dependent. ε_p^o is a constant equal to 0.001 [23,35]. The constitutive
243 parameters of an AA7050 at sub solidus temperature has been obtained in our previous work [24]. In
244 this work we set $T_{merge} = 410$ °C and $T_0 = 390$ °C as suggested by Lalpoor et al. [23]. The nomenclature of
245 each variable in the equations is shown in Table III.

246

247

248

Table III Nomenclature.

T	Temperature
g_s	Volume fraction solid
$\boldsymbol{\tau}_s$	Deviatoric part of stress tensor
$\bar{\sigma}_s$	von Mises stress
$\dot{\boldsymbol{\varepsilon}}_s^p$	Viscoplastic strain-rate tensor
$\dot{\varepsilon}_s^p$	Effective viscoplastic strain-rate
ε_s^p	Viscoplastic strain
X	Stress triaxiality
α, C^*	Internal variables function of g_s and X
$p, \alpha_0, \alpha_1, X_0, \Delta x, \Delta g_s, k$	Semi-solid parameters of cohesion model
$\sigma_0, \dot{\varepsilon}_0, Q, n$	Parameters of high-temperature solid-state creep law
K, r, m	Parameters in extended-Ludwik equation (ALSPEN) constitutive model
R	Molar gas constant
g_s^{coh}, g_s^{coal}	Coherency and coalescence solid fraction respectively
I	Identity tensor

249

2.3 Constitutive parameters extraction procedure

251 To describe the semi-solid properties of the alloy, ALSIM uses the constitutive equations described in
252 [21,28]. The internal functions of the semi-solid constitutive equation (Eq. 1 – 5) show that the
253 constitutive parameters that needs to be extracted and optimized are the rheological parameters p,
254 α_0, α_1, gs$_{coal}$ and k. Since the parameters of solid part of the alloy (represented by creep law properties
255 – Eq. 7 and 8), i.e. $\sigma_0, \dot{\varepsilon}_0$, Q and n have been obtained in our previous work [24], in this study we focus
256 on obtaining the constitutive parameters for the semi-solid part of the constitutive model by utilizing
257 ALSIM package.

258 The flow chart of the constitutive parameter extraction procedure is shown in Figure 3. As a
259 prerequisite, two sets of information have to be obtained experimentally. The first set of information
260 is the tensile force-displacement curves of the alloy at different solid fractions. The second required
261 set of information that is the temperature distribution across the length of the sample at various solid
262 fractions where the isothermal tensile tests mentioned in the previous point have been carried out.
263 After we possessed the necessary information, two steps need to be done for obtaining the
264 constitutive parameters of the alloy. We start by making a temperature distribution model using
265 ALSIM and verify the simulation results with the experimentally measured temperature. Then, using
266 the sample geometry with modeled temperature distribution, we carry out numerical tensile tests and
267 find the constitutive parameters that have the best fit with respect to the experimental tensile test
268 data (lowest value difference between numerical and experimental force-displacement curves).

269 It is necessary to build a temperature distribution model across the sample because the length of the
270 semi-solid regime is different at various test temperatures. In high-temperature mechanical test,
271 deformation mostly occurs in the weakest part of the sample, i.e. in this case, at the semi-solid region
272 because this part is significantly weaker compared to the fully solid part [36,37]. Thus, a realistic
273 temperature distribution along the sample is critical for obtaining accurate constitutive parameter
274 values. We built a simple thermal model of the sample using ALSIM which focuses on the main heat

275 transport phenomena: heating by induction coil and cooling by both a water-cooled surface and air
276 cooling from the ambient temperature. This model aimed at depicting the steady-state temperature
277 distribution along the sample length where the central part of the sample had the test temperature
278 while heat was constantly extracted by the cooling surfaces.

279 To reduce the calculation time, we made a 2D thermal model, by taking an axial cross-section of the
280 sample. However, due to axis-symmetry and for efficiency, only a quarter-part of the cross-section is
281 simulated. The sample geometry was taken from the gage-length of the sample, represented as a
282 sample longitudinal cross-section with a length of 50 mm (from the mid-length to just before the notch
283 – see Figure 2) and a width of 5.84 mm. To simulate heat generation, which in the experiment was
284 done by induction heating, a layer of a source-term was specified (a specific region in the simulation
285 geometry that injected heat to the system) in the surface area around the mid-length of the sample.
286 The power given by the source-term was regulated in such a way that the temperature in the central
287 mid-length of the sample resembled the test temperature. To depict heat extraction phenomenon,
288 the main heat extraction came from the cooling surface at the end of the sample and the secondary
289 heat extraction was by the air cooling from the sample surface. The water temperature and ambient
290 room temperature resembled the experimental conditions: water temperature was 8 °C and room
291 temperature, 20 °C. The illustration of the thermal model and its parameters is shown in Figure 4. The
292 results obtained with this model were then compared to experimental temperature measurements
293 specifically done for this purpose (no mechanical deformation was performed on the temperature
294 calibration measurements). These tests were done with conditions corresponding to some of the test
295 temperatures specified in Table II. In the experiment, we measured the temperature at 4 different
296 points; at 0 mm, 12 mm, 24 mm and 39 mm-off the mid-length along the length of the sample.
297 Additionally, we also obtained the radial temperature distribution of the sample by measuring the
298 temperature at the central mid-length and 5 mm off-center in the mid-length of the sample. From
299 these measurements, we adjusted the model parameters (dimension of the source term, water heat
300 transfer coefficient or HTC_{water} and heat transfer coefficient to ambient temperature or HTC_{air}) such
301 that a good qualitative fit between the model and the measured temperature was obtained. The
302 obtained parameters are presented in Section 3.

303 After the temperature distribution across the model geometry has been obtained through the
304 numerical model, such a geometry was used as a template for the numerical tensile test at different
305 solid fractions. The numerical tensile test model was also built using ALSIM which includes a semi-solid
306 mechanical model. The tensile displacement-rate used on the simulation is half of its experimental
307 counterpart because the geometry of the simulation is only half the total gauge length of the
308 specimen. To describe the solid part of the model (eq. 7 and 8), the parameters obtained in our
309 previous work were used [24]. For the semi-solid part, we used the Al-2% Cu semi-solid database [28] as
310 an initial guess, due to its availability and its similarity to AA7050 in terms of HT susceptibility [9]. Using
311 this combination of databases, we carried out the numerical tensile tests and then compared the value
312 between the numerical and experimental force-displacement results. The aim was to have minimum
313 difference between these two curves. Thus, we varied the semi-solid constitutive parameters and then
314 execute the numerical tensile tests again until a good qualitative fit was achieved between numerical
315 test results with its experimental counterpart. However, since the constitutive parameters that need
316 to be fitted are not solid-fraction nor temperature dependent, a unique set of parameters (i.e. p, α_0,
317 α_1, gs_{coal} and k) that yields a reasonable global error for all solid fractions in the semi-solid regime
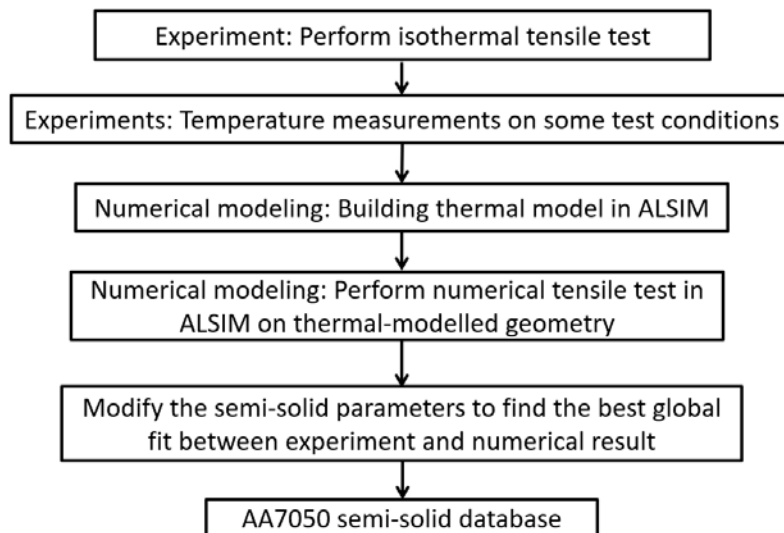318 needs to be obtained.

10

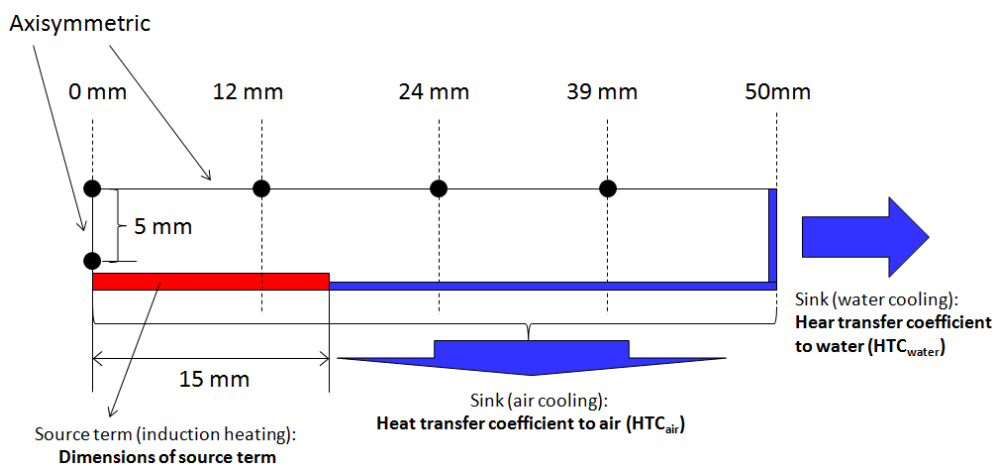Figure 3 Flow chart of semi-solid constitutive parameter extraction using ALSIM.

319

Figure 4 Thermal model illustration along with model parameters. The black dots represent the temperature measurement points on both experiment and numerical model.

320

321 **3. Results**

322 **3.1 Tensile mechanical behavior**

323 Figure 5 shows that the alloy strength increases with solid fraction (decreases with increasing
324 temperature) for both low (0.2 mm/min - Figure 5a,b) and high (2 mm/min - Figure 5c) displacement
325 rates, as have been briefly presented in our previous work [36]. Additionally, from Figure 5a, b we
326 observe two mechanical property transitions. First, the alloy behavior changes from ductile at f_s = 1.0
327 (T = 465 °C) to brittle at f_s = 0.97 (T = 473 °C). The sharp drop in the ability of alloy to accommodate
328 deformation and strength at f_s = 0.97 (T = 473 °C) informs us that the alloy fails in a brittle manner.
329 The second transition in the mechanical behavior of the material occurs when the solid fraction of the
330 alloy decreases from f_s = 0.97 (T = 473 °C) to f_s = 0.85 (T = 550 °C). As the solid fraction decreases, the
331 end part of the curve (post-peak part of the curve) changes (e.g. the post-peak slope at f_s = 0.85 (T =
332 550 °C) is not as steep as at f_s = 0.97 (T = 473 °C)), and the slope gradually becomes shallower and start
333 to have 'tail' after the sharp drop. Finally, at the lowest solid fraction in this test series (f_s = 0.85, T =
334 550 °C), the curve resembles a shallow symmetric hump with a long 'tail'. A similar change in the force–

11

335 displacement curve is also observed at a displacement rate of 2 mm/min (Figure 5c). Figure 5d shows
336 an example of test repeatability at the lowest solid fraction from the test series: f_s = 0.85 (T = 550 °C).
337 We can see that the load-displacement curves are generally grouped together especially from the load
338 building phase up to the displacement of 0.3 mm (shortly after the peak force reached) and diverges
339 afterwards. The force value difference between different tests is relatively low (within approximately
340 5 N). This shows the high quality of the test results despite the presence of significant liquid fraction
341 in the sample.
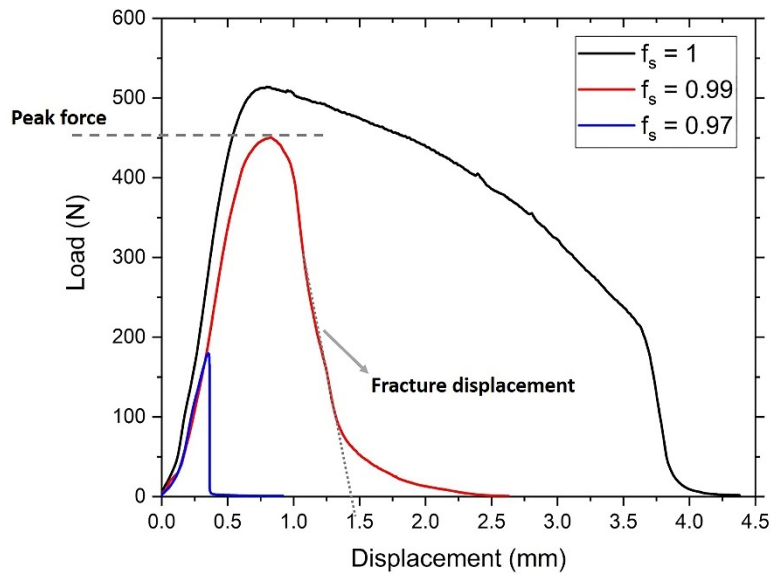
(a)
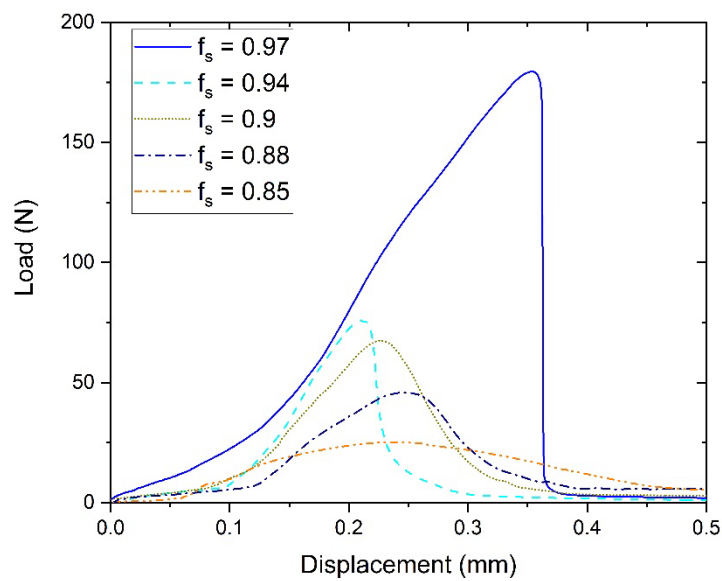
(b)
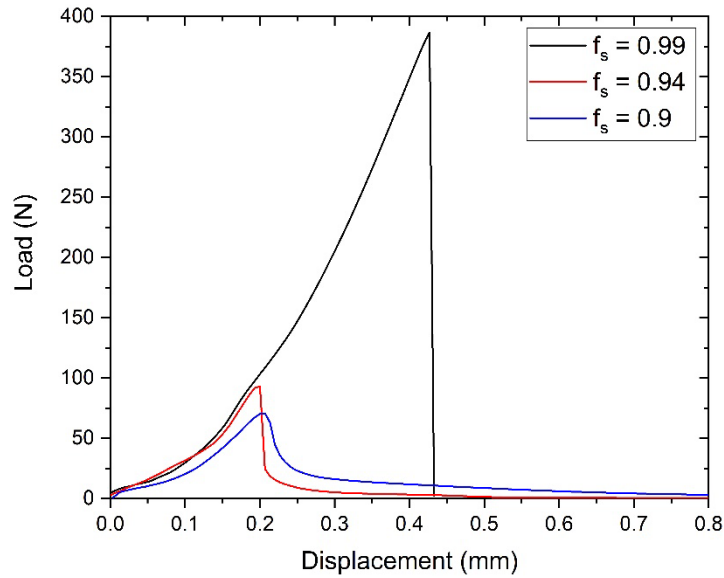
(c)
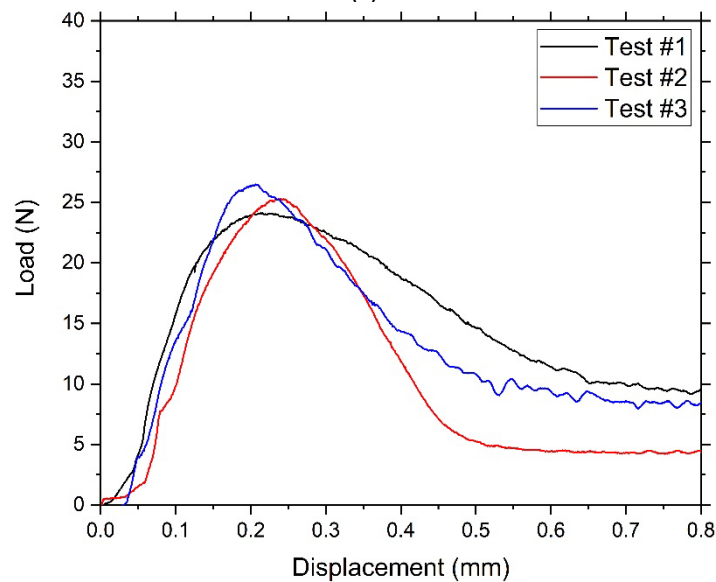
(d)

Figure 5 Force-displacement curves at a low displacement rate (0.2 mm/min) at (a) $f_s \geq 0.97$ or $T \leq$ 473 °C and at (b) $f_s \leq 0.97$ or $T \geq 473$ °C. (c) Force-displacement curves at a displacement rate of 2.0 mm/min (adapted from Ref. [36]). (d) Example of test repeatability at $f_s = 0.85$ (T = 550 °C), with displacement rate of 0.2 mm/min

342   Peak force and fracture displacement are used to quantify the mechanical behavior of the alloy. Peak
343   force is described as the maximum force value in the force-displacement curve and fracture
344   displacement is described as the intersection between the force equals zero axis and the extrapolation
345   of the last linear regime after the peak force before the sample completely failed. An example of both
346   the peak force and fracture displacement is shown in Figure 5a.

347   To relate the peak force value to the strength of material, as an estimation, the peak force value can
348   be converted into an engineering peak stress by dividing this value with the initial sample cross
349   section. The initial cross section was selected because the sample is relatively brittle especially at solid
350   fractions below solidus, thus we assumed that the area reduction before fracture is minimum. Figure
351   6a shows that at a displacement rate of 0.2 mm/min, the minimum engineering peak stress is obtained

13

352 at f_s = 0.85 (T = 550 °C) with a value around 0.23 MPa (25 N) while the maximum engineering peak
353 stress is obtained at f_s = 1.0 with value around 4.92 MPa (527 N). There is a significant increase in the
354 peak force as the alloy is cooled down from 475 °C (f_s = 0.94) to 473 °C (f_s = 0.97). Additionally, for
355 both displacement rates, the peak force rapidly increases as the temperature is lowered below 475 °C
356 (f_s = 0.94). One also notices that the alloy starts to become displacement-rate sensitive at lower test
357 temperature (starting at 475 °C (f_s = 0.94) and below).

358

(a)　　　　　　　　　　　　(b)　　　　　　　　　　　　(c)
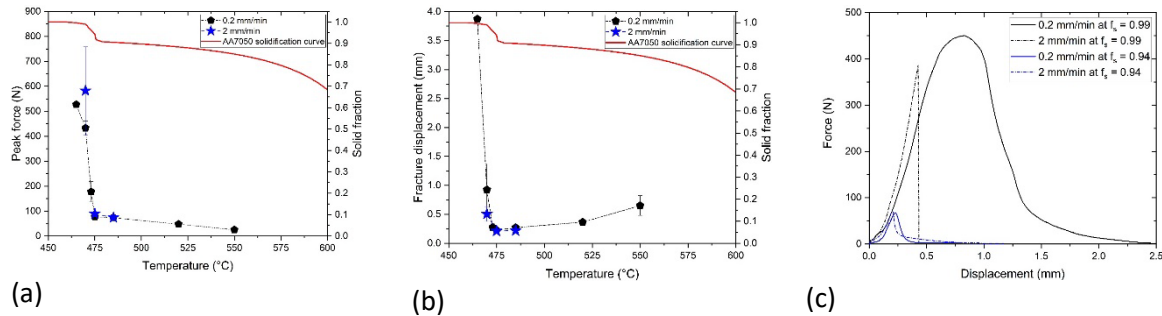
Figure 6 (a) Peak force at different temperatures compared to solid fraction (red line). The
temperature measurement uncertainty is within 0.8 °C. (b) Fracture displacement at different test
temperatures and the comparison with respect to solid fraction (red line), adapted from Ref. [36].
The error bars in these figures represent standard deviations based on three tests. (c) Displacement
rate sensitivity at two solid fractions. Before coalescence (f_s = 0.94 or T = 475 °C) and after
coalescence (f_s = 0.99 or T = 470 °C).

359

360 Figure 6b shows the fracture displacement starts to drop as the test temperature goes above 465 °C
361 (f_s = 1.0) and it reaches the lowest point at 475 °C (f_s = 0.94) for both displacement rates. The alloy
362 starts to be able to accommodate again at test temperatures beyond 475 °C (f_s = 0.94), forming a
363 well-known U-shaped form (see a review in [6]). For both Figure 6a and Figure 6b, each point in the
364 peak force and fracture displacement represents the average of three tests and some of the error bars
365 are smaller than the size of the data points.

366 Figure 6c exhibits marginal strain rate sensitivity observed either through the force-displacement
367 curve (Figure 5a-c) or from other mechanical properties, between the solid fraction of 0.94 (T = 475
368 °C) and 0.99 (T = 470 °C). The main difference in mechanical behavior is that at f_s = 0.99 (470 °C) the
369 tests at 2 mm/min gave brittle behavior while at 0.2 mm/min some tests showed brittle behavior
370 while other tests shows that the alloy able to accommodate some deformation (ductile). At 475 °C (f_s
371 = 0.94), there is a slight change in the curve shape at different displacement rates with the principal
372 difference found in the post-peak curve shape. At the lower displacement rate, the decrease is more
373 gradual compared to the slope at 2 mm/min.

374 **3.2 Fracture surface analysis**

375 SEM fracture surface analysis was performed to reveal the failure mechanisms at different solid
376 fractions. Four samples at different test conditions were observed (i.e. at T = 470 °C (f_s = 0.99) and T =
377 475 °C (f_s = 0.94) and one for each deformation rate) reflecting the transition from brittle to ductile
378 behavior (see Figure 5a,b and Figure 6a,b).

379 The fracture surface analysis informs us that the fracture mode in this semi-solid regime is
380 predominantly inter-granular (dendritic morphology visible at the fracture surface) with some

381 features of fracture going through the solid bridges between dendrites. Figure 7 shows an example of
382 fracture surface observed through SEM – the areas within the blue rectangles represent fracture going
383 through the solid bridges while the area within red ellipses reflects the dendritic intergranular fracture
384 mode. Features that possibly attest for broken solid bridges (encircled by dashed red ellipses in Figure
385 8a) were mostly found starting at f_s = 0.94 (T = 475 °C) and above. At lower solid fractions ($f_s \leq 0.94$ or
386 T ≥ 475 °C) the interdendritic liquid raptures (features within the dashed red ellipses in Figure 8b) are
387 commonly observed irrespective of the displacement rate (therefore only fractures at T = 550 °C or f_s
388 = 0.85, with displacement rate of 0.2 mm/min is shown in Figure 8b). Note that such interdendritic
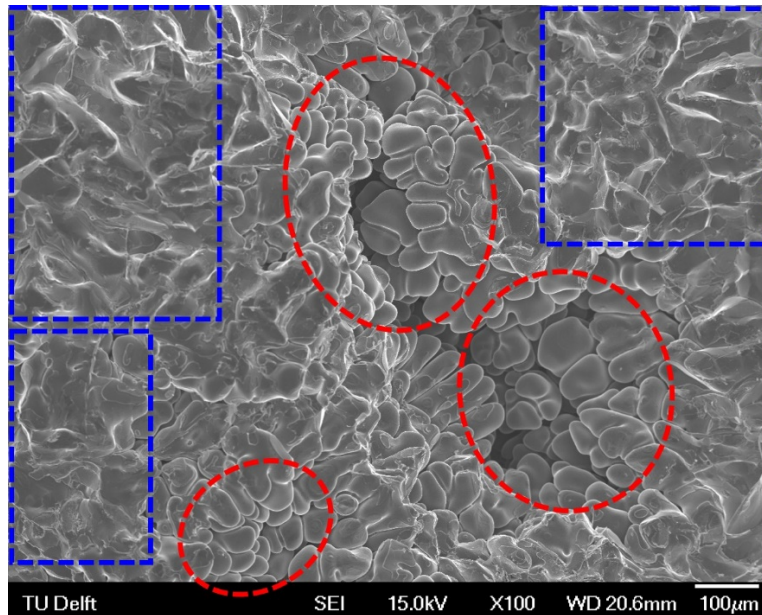389 liquid features are rarely found at the higher solid fractions.

Figure 7 Typical fracture surface observed in the tensile tested samples in the super-solidus temperature regime – mixed fracture mode. Areas within the dashed blue square represent the fracture going through solid phase. While the areas within the dashed red ellipses represent the dendritic intergranular features. This SEM picture is taken from the sample tested at f_s = 0.94 (T = 475 °C) and a displacement rate of 2 mm/min.

390 Figure 8c shows the common morphology of the solidified interdendritic liquid at the higher solid
391 fraction (f_s = 0.99 or T = 470 °C) and slow displacement rate (0.2 mm/min). Meanwhile Figure 8d shows
392 the morphology of the solidified interdendritic liquid phase at similar solid fraction but with at
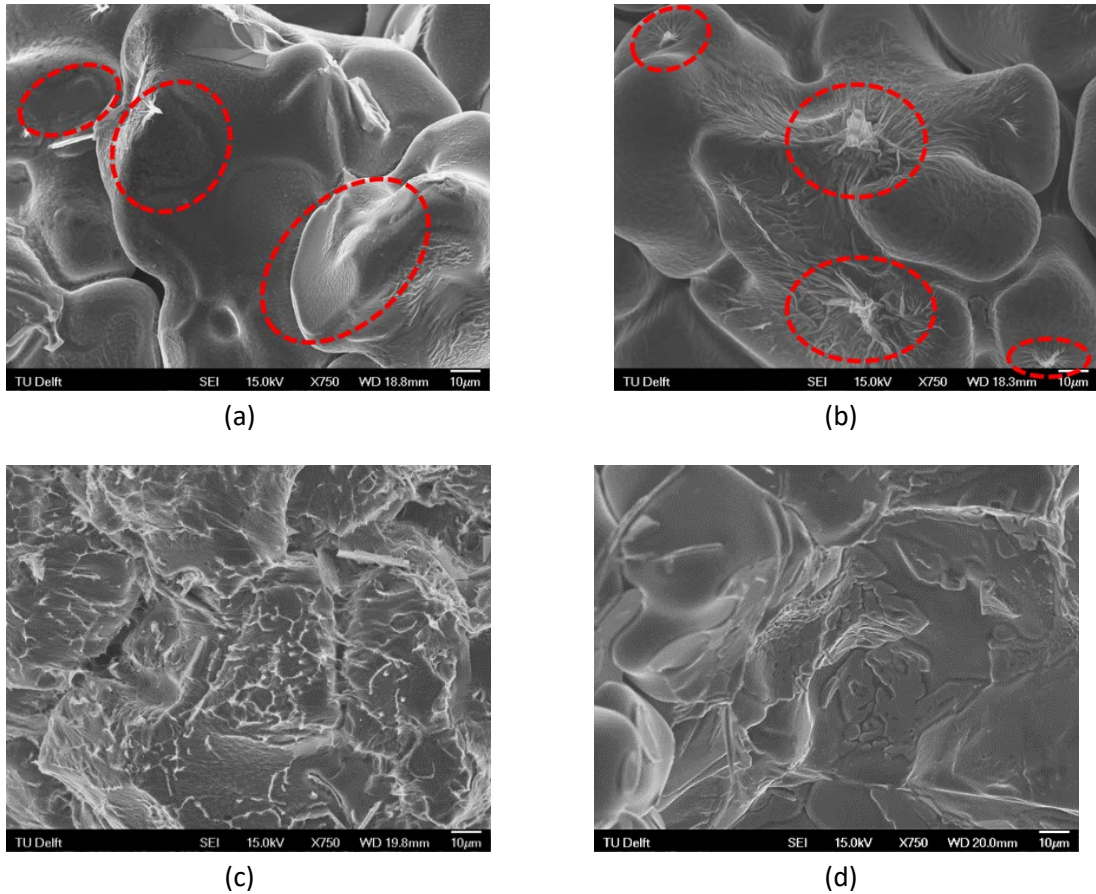393 displacement rate of 2 mm/min.

394

395

396

397

398

Figure 8 SEM fracture surface images at higher magnification. (a) Broken solid bridges (encircled by dashed red ellipses), commonly observed features starting from $f_s = 0.94$ (T = 475 °C) and above. (b) Common feature at lower solid fractions ($f_s \leq 0.94$ or T ≥ 475 °C); broken liquid bridges (drape-like features) encircled by dashed red ellipses. Samples in (a) is tested at 475 °C ($f_s = 0.94$) while (b) is tested at 550 °C ($f_s = 0.85$), both pulled at a displacement rate of 0.2 mm/min.(c) Typical eutectic layer morphology at a higher solid fraction ($f_s = 0.99$ or T = 470 °C) with a displacement rate of 0.2 mm/min and (d) typical eutectic layer morphology at a higher solid fraction but with a displacement rate of 2 mm/min.

399

3.3 Semi-solid constitutive parameters extraction

Temperature field comparison

A good qualitative fit between the thermal model (described in Materials and Methods section) and the measured temperature was achieved when the following settings were used to run the model: (1) The dimensions of the source term: length of 15 mm and width of 0.6 mm. (2) The heat transfer coefficients to water and air-cooling were $HTC_{water} = 1000$ W/m² and $HTC_{air} = 10$ W/m², respectively. Table IV shows the temperature difference between the measured and modeled temperature ($T_{meas.}$-T_{model}) at different test temperatures along the length of the sample using the mentioned model parameters. From this table, the highest temperature difference between the model and the measurement is found at the test temperature of 485 °C ($f_s = 0.9$) instead of at the extremities of the test temperatures (T = 550 °C ($f_s = 0.85$) and T = 460 °C ($f_s = 1.0$)).

Table IV Difference between measured temperature ($T_{meas.}$) and modeled temperature (T_{model}) in the axial length (center of the sample) at different temperatures in the mid-length of the sample.

Dist. From center (mm) / Center temperature	($T_{meas.}$- T_{model}) 12 mm (°C)	($T_{meas.}$- T_{model}) 24 mm (°C)	($T_{meas.}$- T_{model}) 39 mm (°C)
550 °C (f_s = 0.85)	1.4	1.1	-7
485 °C (f_s = 0.9)	-3.9	-9.3	-14.7
473 °C (f_s = 0.97)	-0.6	-2.5	-6.5
460 °C (f_s = 1.0)	0.4	1.6	-4.5

411 Figure 9a (left) shows the temperature distribution where red corresponds to higher temperatures
412 and blue to lower temperatures while the corresponding solid fraction based on the temperature
413 distribution is shown in Figure 9a (right). The result of the model shows that the biggest temperature
414 gradient is along the length of the sample – lower temperature toward the water-cooled surfaces and
415 there is almost no temperature gradient to the radial direction (approximately 2 °C). This finding is
416 supported by the temperature calibration measurement; the temperature difference between the
417 center and 5 mm off the center of the sample mid-length is approximately 2 °C. This shows a good
418 correlation between the temperature measurement and the model.

419

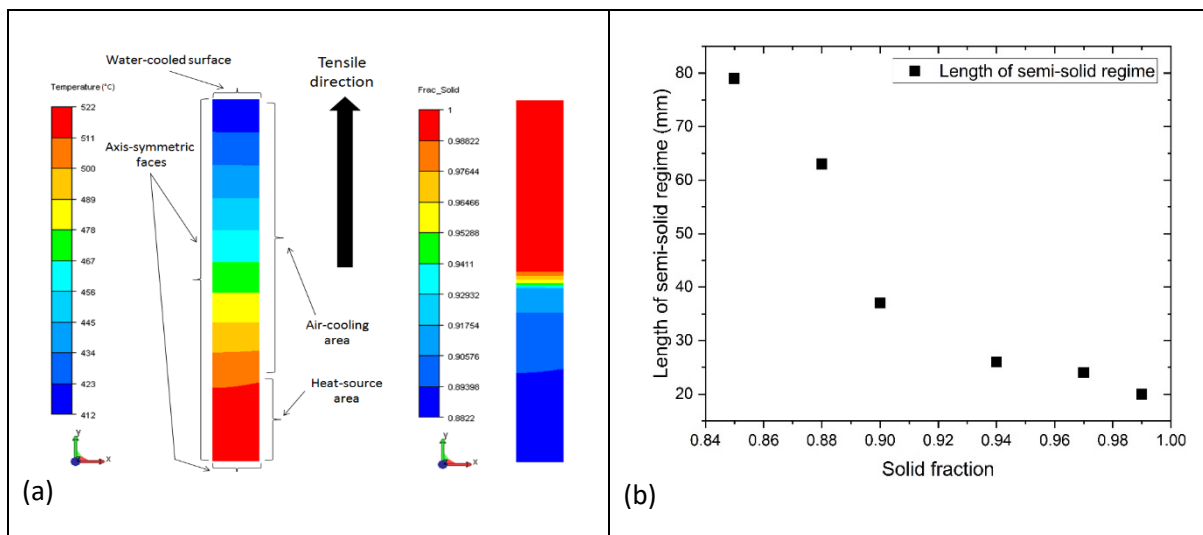Figure 9 Example of thermal modeling using ALSIM when the center of the sample is at f_s = 0.88 (T = 520 °C). (a) Comparison between temperature (left) and solid fraction (right) distribution. (b) Length of semi-solid regime for the entire gage-length of the sample (double the length of the model geometry) for different solid fraction based on thermal model.

420

421 Thermal modeling result enables us to estimate the length of the semi-solid region in the sample as
422 shown in Figure 9b. The semi-solid region is defined as the length between the mid-length of the
423 sample and the solidus point (f_s = 1.0 or T = 465 °C). The trend shows that the length of the semi-
424 solid regime decreases as solid fraction increases with a significant drop occurring between f_s = 0.88
425 (T = 520 °C) and f_s = 0.9 (T = 470 °C).

426

427

Numerical vs. experimental tensile test

The numerical tensile test in ALSIM takes place with the geometry that has been temperature modeled as described in the previous section. As the radial temperature distribution found to be insignificant, for simplicity, in the mechanical part of the simulation we only use the axial temperature distribution along the sample. An example of comparison between the solid fraction and the effective strain distribution in the sample of a numerical tensile test at a solid fraction of 0.9 (T = 485 °C) is shown in Figure 10. This figure shows that most of the strain takes place in the semi-solid part of the sample (the region of the sample where solid fraction is below 1.0 or T = 465 °C).
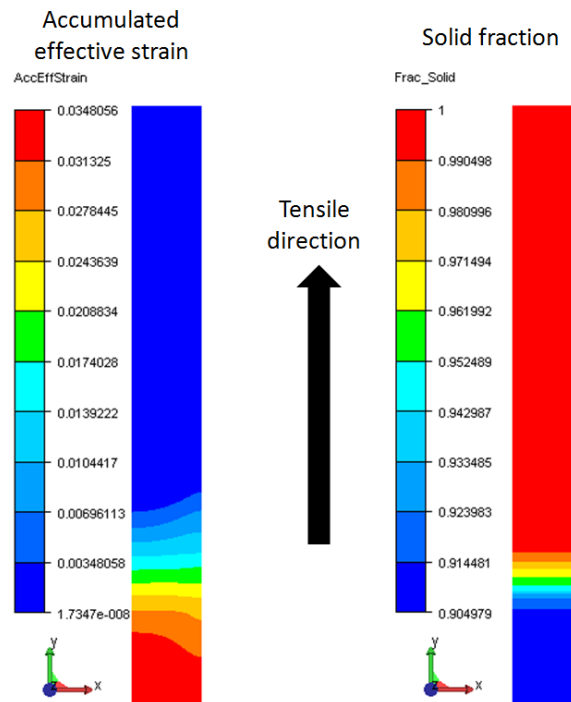

Figure 10 (left) Example of strain calculation result at f_s = 0.9 (T = 485 °C) in comparison to (right) the location of the semi-solid regime based on the solid fraction distribution.

Figure 11a shows that the semi-solid constitutive model substantially captures the load development part of the curve. However, the semi-solid parameters are not solid fraction (or temperature) dependent, thus only a reasonable global minimum error is expected. Examples of a global fit of the semi-solid parameters plotted at different solid fractions and compared to their experimental counterparts are shown in Figure 11b. This figure illustrates that the results from numerical tests underestimate the experimental forces from f_s = 0.9 (T = 485 °C) and below, while the results from numerical tests tend to be overestimate the experimental forces above f_s = 0.9 (T = 485 °C).

Constitutive parameters

From the method shown in previous section, we obtained semi-solid constitutive parameters for the AA7050 alloy shown in Table V in comparison with those of two other alloys that can be found in references. The result shows AA7050 has the lowest 'p' value while having the highest value of 'α_0' and the value of 'α_1' is between those of the other two alloys.
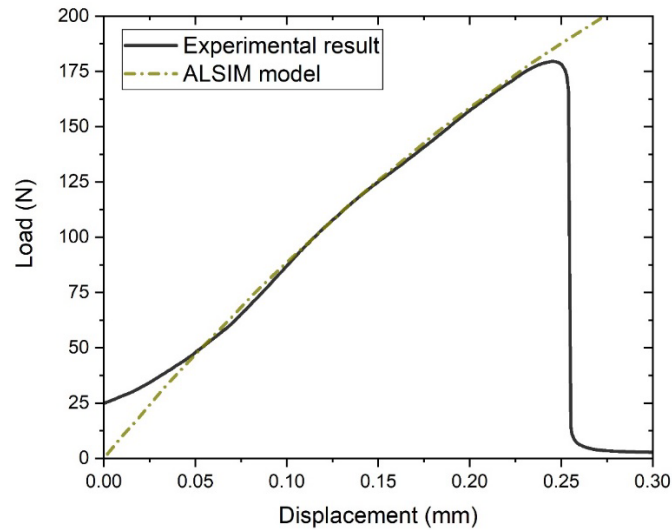
(a)
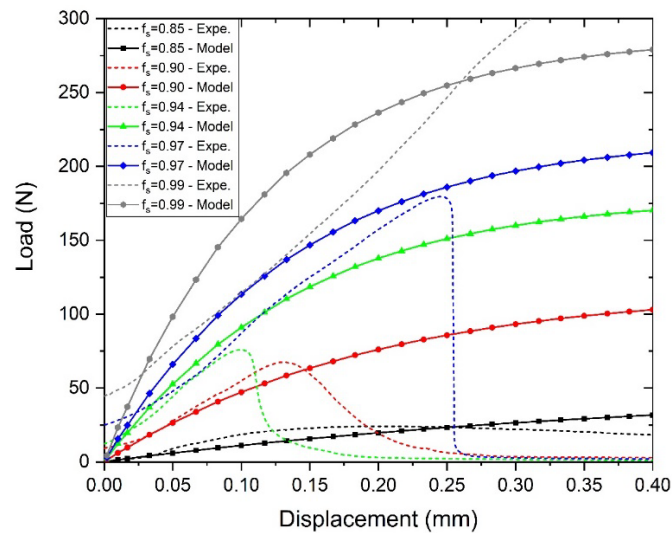
(b)

Figure 11 (a) An example of an individual (single-curve fit) comparison between numerical tensile test (red line) and an experimental data (blue line) at f_s = 0.97 (T = 473 °C) and a displacement rate of 0.2 mm/min. (b) Examples of simultaneous fitting at different solid fractions (global fit).

448

449 Table V Comparison of the AA7050 semi-solid constitutive parameters with those for different alloys
450 described using ALSIM semi-solid constitutive equation (Eq. 3 – 5).

Parameters Alloys	p	α_0	α_1
AA5182 [27,29]	0.315	10.54	0.0632
Al–2% Cu [28]	0.11	4.45	0.0107
AA7050 (this work)	0.08	13.65	0.0116

451

452 To compare the semi-solid constitutive behavior of different alloys in terms of tensile force-
453 displacement curves, we plot the tensile response for each alloy shown in Table V using numerical
454 tensile test setup in ALSIM (shown in the previous section). Numerical tensile tests were carried out
455 at different solid fractions with deformation speed mimicking the tensile test at the lower
456 displacement rate (0.2 mm/s).
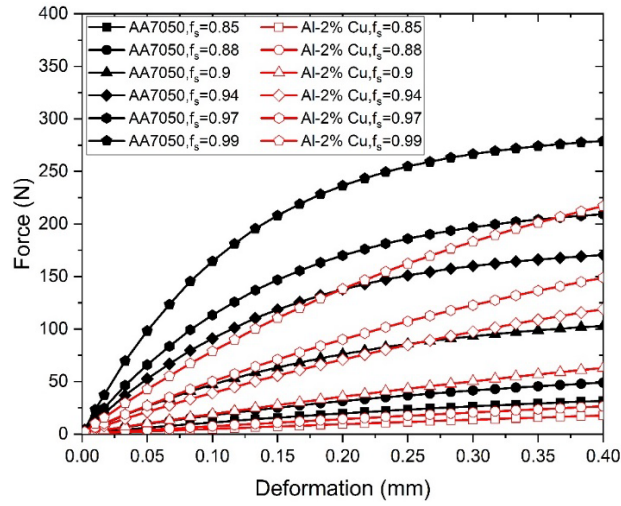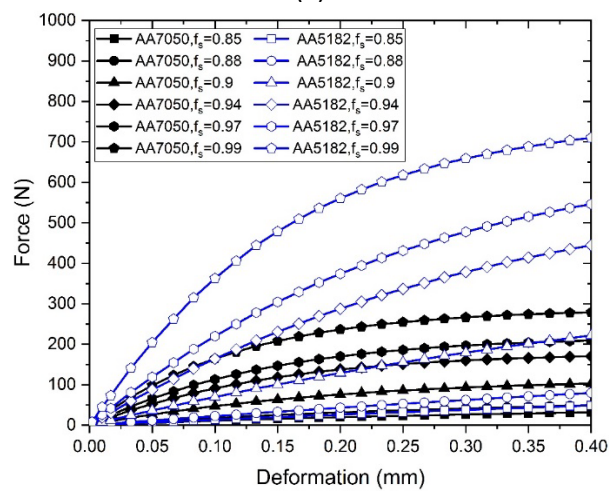
Figure 12 (a) Comparison of modeled tensile response at different solid fractions between Al–2% Cu (red lines with hollow markers) and AA7050 (black lines with solid markers). (b) Comparison of modeled tensile response at different solid fractions between AA5182 (blue lines with hollow markers) and AA7050 (black lines with solid markers lines).

457   Subsequently we compared the result of the numerical tensile tests of AA7050 with two different
458   alloys described in Table V, and the outcome is depicted in Figure 12. The result shows that in the
459   semi-solid state, AA7050 alloy is stronger than an Al–2% Cu alloy (Figure 12a) but it is weaker that the
460   AA5182 alloy (Figure 12b). It is clear that the strength and load development characteristics (the rate
461   of the alloy to reach high force values with respect to displacement) are dissimilar for the three
462   different alloys. The difference in both strength and behavior becomes more significant as the solid
463   fraction increases, especially starting above f_s = 0.88 (T = 520 °C). In terms of strength, the AA7050
464   alloy is comparable to the Al–2% Cu alloy but the load development characteristic is clearly different
465   – AA7050 alloy is quicker to reach high force values compared to Al–2% Cu which has a slower load
466   development mode. In comparison with AA5182, the AA7050 alloy has a relatively similar load
467   development characteristic – relatively quick increase in load at lower displacement and saturation as
468   the displacement increases. However, it is clear that the semi-solid AA5182 alloy is stronger than the
469   AA7050, especially at higher solid fractions.

470   **4. Discussion**

20

4.1. Semi-solid mechanical properties

It is well known that the structure affects the semi-solid mechanical properties and hot tearing susceptibility, see for example a review in Ref. [6]. However, the structure parameters such as grain size and dendrite arm spacing become important when their variation is rather strong [7]. Under conditions when the entire sets of samples undergo the same testing procedure (as in our experiments), the difference in structure features are expected to be minimum, as their effect on the properties. In a selection of papers similar in methodology to our paper, the structure factor has not been taken into account for these reasons, e.g. [38–40] showed that the effect of structure defects is much stronger than the structure parameters such as grain size and dendrite arm spacing. Therefore, we assumed that the structure factor in the mechanical behavior of the samples tested in this work was not influential. The amount of the liquid phase and its distribution had more decisive effect.

From the evolution of the force-displacement curves at different solid fractions shown in Figure 5a-c, we can deduce the mechanical behavior of the alloy at different solid fractions and relate it to the solidification process. Generally, the evolution of the mechanical behavior is comparable with the solidification process described in previous works [5,6,25,41]; at the beginning of solidification until the coherency temperature, when there is still a significant amount of liquid in the system, the alloy is fluid, i.e. very "ductile". At a lower temperature, when feeding becomes difficult, the alloy becomes brittle and prone to HT. After the dendrites have merged together, the alloy acquire strength to resist thermal stress, acquiring the ability to accommodate deformation, albeit very small one. This behavior is commonly observed in various alloys and is described as a brittle or vulnerable temperature range that is linked to the HT susceptibility of the alloy [6]. Moreover, the shape and evolution of the force-displacement curves obtained in this work by tensile testing is similar to those reported on other alloys [6,27]. As the solid fraction decreases, the length of the force 'tail' (after the force-displacement curve reaches the peak force) increases irrespective of displacement rate used for the test. This might be caused by the increasing presence of the liquid phase within the sample during the test. The liquid and some solid bridges between grains continue to hold them together, extending and deforming, creating a fictional elongation despite the fact that the sample is already fractured [6].

From the result in Figure 6a, we observe a stark increase in the engineering peak stress from solid fraction of 0.94 (T = 475 °C) to 0.97 (T = 473 °C) which signifies that the alloy become more resistant to HT formation starting from f_s = 0.94 (T = 475 °C). Meanwhile, Figure 6b illustrates the alloy is brittle in the temperature range between solid fractions of 0.9 (T = 485 °C) and 0.97 (T = 473 °C), therefore the entire test at f_s = 0.94 (T = 475 °C) occurs in the range of the minimum ductility. This also corresponds to the suggestion given in the previous work [26]; liquid feeding stops at approximately f_s = 0.9 (T = 485 °C) but at this solid fraction the grains have not yet coalesced, therefore the semi-solid material is not yet sufficiently strong to resist developing HT. As the solidification progresses, after passing the most brittle point (at f_s = 0.94 or T = 475 °C), the alloy starts to be able to accommodate deformation again, which could be interpreted that from this this solid fraction on, the microstructure is able to accommodate deformation before HT occurs. This phenomenon resembles the occurrence of grain coalescence as reported elsewhere [26]. This value is supported by other works on different aluminum alloys that grain coalescence in aluminum alloy typically occurs between f_s = 0.94 (T = 475 °C) and 0.97 (T = 473 °C), such as in AA6060[41], AA6061[26], AA6056[30], Al-1%Cu[42], Al-2%Cu[28], and AA5182[29].

In terms of deformation rate sensitivity, there were not many differences observed in terms of the force-displacement curve shape (Figure 6c), peak force (Figure 6a) or fracture displacement Figure 6b) for tests conducted with different displacement rates. This may be correlated to the similarities of the fracture surface features at both solid fractions; below (at f_s = 0.94 or T = 475 °C) and above grain

21

517   coalescence (at f_s = 0.99 or T = 470 °C) as illustrated in Figure 7 and Figure 8. However, the difference
518   in peak stress and fracture displacement at different displacement rates starts to increase with solid
519   fraction. This might be because at higher solid fractions, there are already more solid bridges
520   connecting the dendrites (e.g. features shown in Figure 7 and Figure 8a), thus the alloy behavior
521   approaches the sub-solidus regime characteristics (presence of positive [38] and increased [24] strain-
522   rate sensitivity as temperature decreases within this temperature regime). Additionally, this condition
523   can also be linked with the increase of error-bar width with solid fraction. This may indicate that at
524   higher solid fractions in the semi-solid range, the alloy strength does not only depend on the solid
525   fraction but also on the distribution of the formed damage and/or eutectics at the grain boundaries.

526   **4.2. Failure behaviour**

527   Fracture surface analysis also presents some interesting observations. For instance, the mixed fracture
528   surface features, e.g. dendritic intergranular fracture (within red ellipses in Figure 7) and fracture
529   through the solid phase (within blue squares in Figure 7), were found irrespective of the solid fraction
530   and displacement-rate during the test. One possible explanation for this phenomenon is that the
531   dendritic intergranular features are a result of separation of the grains completely covered by the
532   liquid while the fracture can also go through the solid bridges between grains in agreement with HT
533   mechanisms [5]. Therefore, the possible reason for these mixed fracture-features observed in our study
534   is because even at the lowest studied solid fraction (f_s = 0.85 or T = 550 °C), the alloy has already
535   transmits an appreciable load (Figure 5b). This means some of the dendrites are already linked
536   together (and able to transmit loads), thus, the separation of dendrites through the solid bridges is
537   possible. Areas within red ellipse in Figure 8a exhibit features that resembles ductile fracture of solid
538   bridges which is commonly observed at higher solid fraction where grains have welded together [29].
539   On the lower solid fraction side, i.e. below coalescence point (f_s ≤ 0.94 or T ≥ 475 °C), broken liquid
540   films (drape-like features) as shown in Figure 8b. Such a morphology is also observed in previous works
541   on semi-solid deformation [43,44]. One possible explanation on the formation of such a feature would
542   be: when there is sufficient liquid phase in the system, and mechanical deformation occurs leading to
543   grain separation, the liquid phase clings to the surface of the moving grains held together by surface
544   tension and gradually solidifies, thus leaving spikes and tails. This also explains the lesser prevalence
545   of such a morphology at higher solid fractions, because sufficient amount of the liquid phase is needed
546   at the grain boundaries to form such drape-like features.

547   Another interesting fracture surface feature that we observed is that at the high solid fraction (at f_s =
548   0.99 or T = 470 °C), the morphology of the eutectic is deformation-rate dependent (Figure 8c, d). The
549   tests at a lower displacement rate (0.2 mm/min) show that the former eutectic is more elongated and
550   produces filament-like features. This feature has been also observed in the higher temperature
551   portion of the sub-solidus regime (commonly visible starting at 455 °C [24,37]) at a strain-rate of 0.0005
552   s^{-1}. This could be explained as the micro-superplasticity behavior observed by Takayama et al. [45] in an
553   AA7475 alloy near the solidus temperature. The morphology of the micro-superplasticity feature in
554   Figure 8c is comparable to the morphology reported at the moderate strain-rate given in Takayama et
555   al.'s work ($2.8 \cdot 10^{-3}$ s^{-1}) which is more related to the slower displacement rate (0.2 mm/min) we use
556   in the semi-solid regime tensile test. The whiskers produced in the tests at T = 470 °C (f_s = 0.99) are
557   shorter compared to the tests at 465 °C (f_s = 1.0) at 0.0005 s^{-1} [24]. This can be explained by the trend
558   of superplasticity given in previous works [26,45] that the length of the filaments inversely proportional
559   to the pulling speed because if the displacement rate is too high, the viscous flow becomes unstable
560   and the filament cannot form. This may be the reason the length of the filament that we found in this
561   work is relatively short compared to the result by Giraud [26] in the AA6061 alloy at a faster pulling
562   rate. However, another thing that needs to be taken into account is that in terms of chemical

563 composition, AA6061 is quite different than the AA7050 alloy, whereas that difference is less
564 compared to AA7475-type alloys.

565

566 **4.3. ALSIM Numerical model**

567 The thermal model that we built using ALSIM shows that the most sensitive parameters influencing
568 the temperature distribution along the axis of the sample are the heat transfer coefficient (to water-
569 cooled surface) and the dimension of the heat-source. This is in accordance with the theory since the
570 main thermal influence in the experiment is the heat generated by the heating-coil and heat extraction
571 by the water- and air-cooled surface. From the comparison between the temperature calibration
572 measurement and the thermal model in Table IV, we see that the difference is relatively small up to
573 two thermocouples off the mid-length (12 mm and 24 mm from the mid-length). These two points are
574 considered important because most of the semi-solid regime is formed within this part of the sample
575 especially at solid fractions important for HT development – above f_s = 0.9 (T = 485 °C) the length of
576 semi-solid regime is below 24 mm (Figure 9b). The result demonstrates that a simple thermal model
577 could be utilized to perform a constitutive parameter extraction with reasonable quality. Thus, for
578 development of semi-solid database for other alloys, we may be able to reduce the need to perform
579 temperature calibration measurements at every solid-fraction where the tests are carried out (i.e. we
580 only need to do thermal calibration measurements at the highest and the lowest test temperatures),
581 which ultimately saves time and resources. For future development of the thermal model, we suggest
582 increasing the level of realism in the model, for example, by using a temperature (or solid fraction)
583 dependent heat transfer coefficient as it may increase the simulation accuracy [46].

584 Figure 11a shows that the semi-solid constitutive model in ALSIM can capture the important parts of
585 the force-displacement curve such as the load development part up to the peak force. This figure
586 confirms that a good fit between experimental and numerical force-displacement curve in an
587 individual fit can be obtained. However, for the global fit (Figure 11b), at lower solid fractions (f_s < 0.94
588 or T > 470 °C) the simulated force is underestimating the experimental result while it is the other way
589 around at higher solid fractions. This indicates a compromise in accuracy (from each individual fit) that
590 has to be made to obtain a set of parameters that produce global minimum error. The shapes of the
591 constitutive model curves however, closely resemble experimental curve shapes only at certain solid
592 fractions (Figure 11b); the shape of the force-displacement curves having reasonable fit below a solid
593 fraction of 0.99 (T = 470 °C), where the HT initiation process mainly occurs. These solid fractions
594 (between 0.85 (T = 0.9 °C) and 0.97 (T = 473 °C)) are the most critical part for HT formation as in this
595 regime, feeding starts to become bad but grains has not yet coalesced, thus it is important that the
596 model is able to represent this regime accurately. Above solid fraction of around 0.97 (T = 473 °C), the
597 grains typically have coalesced and thus HT initiation becomes less likely (fewer liquid is available to
598 serve as initiation points [5,47]), thus less accurate representation of the experimental tensile profile by
599 the model is acceptable. The global fit quality is comparable with the results obtained for other alloys
600 using a similar constitutive equations, such as Al-2% Cu [28] and AA5182 [29].

601 The current semi-solid constitutive model in ALSIM is able to reasonably capture the semi-solid
602 behavior of aluminum alloys, especially at the load development phase. However, Figure 5a-c and also
603 other works on tensile semi-solid constitutive behavior of aluminum alloys [28,29] show that damage
604 development phase (the decrease in force value after peak is reached) is also important because it is
605 directly linked to the propagation of the formed HT. Therefore, an implementation of damage
606 development model, for instance the de-cohesion model developed by Mihanyar et al. [48] would be
607 an ideal pathway for further ALSIM model development.

4.4. Constitutive parameters and hot tearing susceptibility

The result of the semi-solid constitutive parameter extraction in Table V indicates that the AA7050 alloy has distinct parameters and consequently different mechanical behavior, as compared to the two other alloys for which the data is available for the ALSIM semi-solid model (i.e. AA5182 [27,29] and Al–2% Cu [28]). The internal variables; C^* (function of p) and α (function of α_0 and α_1) characterize the cohesion rate (Eq. 2) of the alloy during the solidification process and ultimately can be related to the strength of the alloy. This explains the results of numerical tensile simulation shown in Figure 12a and Figure 12b; semi-solid AA7050 is weaker than AA5182 but stronger than Al-2% Cu. This agrees with other experimental results from other alloys (i.e. for Al-2%Cu the maximum tensile strength at f_s = 0.98 is just above 3 MPa [28], while for AA5182 at f_s = 0.96 has a maximum tensile strength of almost 7 MPa [29]). As a comparison, the AA7050 in our study has a maximum engineering tensile strength of approximately 5.47 MPa at f_s = 0.99 (T = 470 °C).

The fact that the AA7050 alloy has lower k values compared to the other aluminum alloys (i.e. AA5182 [29] and Al-2% Cu [28]) shows that for AA7050 (in the tensile stress mode), the strength increase around the grain coalescence point occurs more gradually.

In general, for billet/ingot castings, Al–2% Cu [28,49,50] and AA7050 [23] are known to be susceptible to HT. Based on previous studies [5,6,12,17,25,51], alloys that are susceptible to HT not only have wide solidification range, but also have a higher thermal contraction onset temperature (starting at lower solid fractions). Additionally, tensile mechanical strength in the semi-solid state seems to be also critical as it defines the capability of an alloy to resist HT development. To exemplify this notion, please consider the comparison between Al-2%Cu and a commercial AA5182. An Al–2% Cu alloy has a relatively wide solidification range (around 107 °C where the alloy is fully solidified at about 548 °C – based on JMAT Pro calculation) and the high thermal contraction onset temperature (starting at approximately at f_s = 0.9 [51]). Meanwhile, AA5182 has a wider solidification range (around 185 °C where the alloy reached fully solid state at approximately 450 °C – based on JMAT Pro calculation) compared to the Al–2% Cu alloy, but AA5182 has a lower thermal contraction onset temperature, which corresponds to higher fraction solid (around f_s = 0.95 [16]). It is commonly known that Al-Cu alloys are more susceptible to HT as compared to AA5182 [51,52].

In comparison, AA7050 has a relatively wide solidification range (approx. 170 °C with fully solid state reached at around 465 °C – Figure 1) but has the lowest fraction solid at the onset of thermal contraction (f_s = 0.83 or at 559 °C [15]), therefore its vulnerable range (between the onset of thermal contraction and the nonequlibrium solidus [6,17,51]) is larger than that of both Al–2% Cu and AA5182. Additionally, in terms of the semi-solid mechanical strength, at a lower displacement (i.e. strain), where it is relevant to DC casting [29], AA7050 is weaker than AA5182 although stronger than Al–2% Cu. From this comparison, we can conclude that AA7050 alloy is severely susceptible to HT, thus optimum process parameters to produce sound billets/ingots through DC casting need to be carefully selected.

The results from ALSIM thermal simulation allow us to approximate the length of the semi-solid regime (Figure 9b), where most of the deformation that contributes to HT development occurs. This information combined with the fracture displacement measurement at each solid fraction (Figure 6b), can be used to obtain an estimation of engineering fracture strain; a ratio between fracture displacement and the length of the semi-solid regime at different solid fractions (Figure 13). A potential utilization of this engineering fracture strain data is a HT susceptibility estimation through the comparison with linear-contraction data from thermal-contraction experiments [10–12,15,16,51,53]. The thermal-contraction data may be converted into a strain value, thus an experimental-based HT susceptibility measure, such as in the works of Novikov [6,25] and Magnin [54], could be obtained. The

24

654 implementation of this criteria in ALSIM would also provide a definitive quantification whether HT
655 took place during casting, which ALSIM is currently lacking at the moment.

656 In this work, we demonstrated that a simple thermo-mechanical model built using ALSIM combined
657 with temperature calibration measurements and experimental tensile test data is a reasonable
658 method to extract constitutive parameters for the semi-solid constitutive model (eq. 1 – 7). The results
659 obtained in this work and our previous work in sub-solidus regime [24] not only completed the database
660 of the AA7050 alloy but also provided an insight into the tensile constitutive behavior, which is
661 necessary for understanding the connection between HT and CC.

662 The need of a material database sensitivity analysis in ALSIM model is also supported by our findings
663 in Table V and Figure 12a that the AA7050 and Al–2% Cu alloys have quite a different semi-solid
664 mechanical characteristics, thus we expect differences in the simulation results. Therefore, with the
665 full data set of the AA7050 alloy in the ALSIM materials database, we expect to have better accuracy
666 of thermomechanical and hot-tearing simulations upon DC casting. Additionally, sensitivity of ALSIM
667 model with respect to different alloys should also been taken into account, as this topic is crucial for
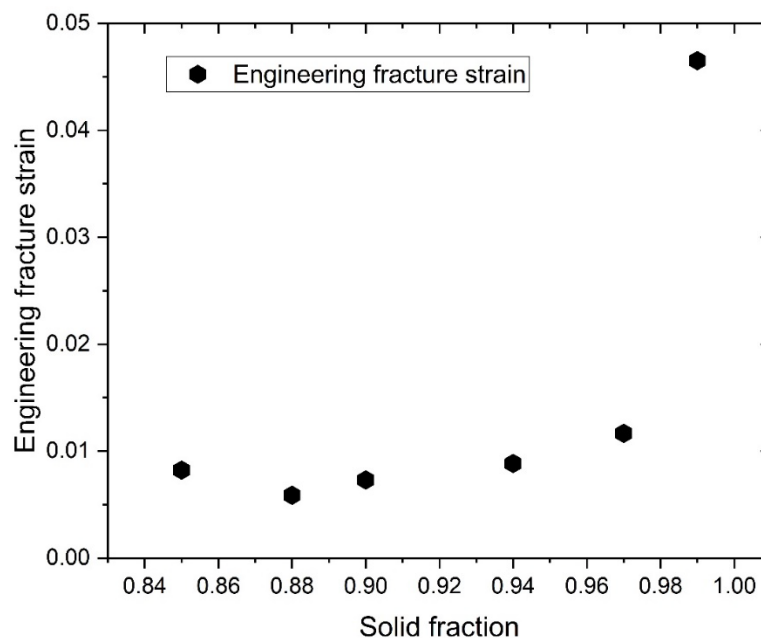668 ALSIM's long-term development.

Figure 13 Engineering fracture strain (strain when fracture occurs) at different solid fractions.

669

5. Conclusions

671 In this work, we have performed a detailed study of the tensile constitutive behavior such as strength
672 (through peak force), ability to accommodate deformation (through fracture displacement) and failure
673 mechanisms of the as-cast AA7050 alloy in the semi-solid state. Additionally, semi-solid constitutive
674 parameters of ALSIM model have been extracted by making a simple thermal model and numerical
675 tensile tests in ALSIM and comparing the simulation result with experimental mechanical test result.
676 The results and analysis that we obtained in this work can be summarized as follows:

677 1. From the shape of the force–displacement curves, we found that in the range of f_s = 1.0 (fully solid,
678 T = 465 °C) to f_s = 0.85 (T = 550 °C), the alloy has three different mechanical behavior regimes: ductile
679 at 1.0 (T = 465 °C) ≤ f_s < 0.97 (T = 473 °C), brittle at 0.97 (T = 473 °C) ≤ f_s ≤ 0.9 (T = 485 °C), and then
680 ductile again (at 0.9 (T = 485 °C) < f_s ≤ 0.85 (T = 550 °C)).

681 2. Grain coalescence for this alloy occurs between f_s = 0.94 (T = 475 °C) and f_s = 0.97 (T = 473 °C), which
682 is signified by the sharp increase in peak force between the mentioned solid fractions.

683 3. Brittle temperature range fracture displacement curve was observed in the semi-solid regime with
684 the alloy being most brittle at 475 °C (f_s = 0.94), and the alloy gains its ability to accommodate
685 deformation again as the liquid fraction increases in the alloy.

686 4. SEM fracture surface analysis revealed that in general the fracture mode is mostly intergranular
687 with fracture propagating through solid bridges as well. Additionally, at higher solid fractions, the
688 morphology of the eutectic is different at different displacement rates (Figure 8c and Figure 8d).
689 Features that depicts ductile fracture of solid bridges between grains were observed in samples tested
690 at higher solid fractions Figure 8a), while sites that resemble necking of interdendritic liquid were
691 observed in samples that were tested at lower solid fractions (Figure 8b), both independent of the
692 displacement rate used during the test.

693 5. Semi-solid mechanical behavior of AA7050 is different to the two alloys with the semi-solid database
694 available for ALSIM (i.e. Al-2%Cu and AA5182). A semi-solid AA7050 alloy is stronger compared to Al–
695 2% Cu but weaker compared to AA5182.

696 6. The HT susceptibility of an alloy is not only influenced by the width of the solidification range but
697 also by the mechanical characteristics in the semi-solid state, such as the fraction solid at the onset of
698 thermal contraction, strength and ductility (ability to accommodate deformation). The results from
699 this study suggest that AA7050 is more susceptible to HT as compared to Al-2%Cu and AA5182 because
700 not only AA7050 has a relatively wide solidification range (170 °C) but the thermal contraction starts
701 at low fractions of solid (f_s = 0.83 corresponding to 559 °C). Moreover, the semi-solid mechanical
702 strength of AA7050 is lower as compared to AA5182.

712

713 **References**

714 1 M. Dixit, R.S. Mishra, and K.K. Sankaran: *Mater. Sci. Eng., A,* 2008, vol. 478, pp. 163–72.
715 2 E.A. Starke and J.T. Staley: *Prog. Aerosp. Sci.*, 1996, vol. 32, pp. 131–72.
716 3 D.A. Granger: *Treatise Mater. Sci. Technol.*, vol. 31, Elsevier, 1989, pp. 109–35.
717 4 N.L. Loh and K.Y. Sia: *J. Mater. Process. Technol.*, 1992, vol. 30, pp. 45–65.
718 5 D.G. Eskin and L. Katgerman: *Metall. Mater. Trans. A*, 2007, vol. 38, pp. 1511–9.
719 6 D.G. Eskin, Suyitno, and L. Katgerman: *Prog. Mater. Sci.*, 2004, vol. 49, pp. 629–711.
720 7 F. Sheykh-jaberi, S.L. Cockcroft, D.M. Maijer, and A.B. Phillion: *J. Mater. Process. Technol.*, 2019,
721   vol. 266, pp. 37–45.
722 8 C. Puncreobutr, P.D. Lee, K.M. Kareh, T. Connolley, J.L. Fife, and A.B. Phillion: *Acta Mater.*, 2014,
723   vol. 68, pp. 42–51.

724   9 Suyitno, V.I. Savran, L. Katgerman, and D.G. Eskin: *Metall. Mater. Trans. A*, 2004, vol. 35, pp.
725   3551–61.
726   10 D.G. Eskin and L. Katgerman: *Mater. Sci. Forum*, 2006, vol. 519–521, pp. 1681–6.
727   11 A. Stangeland, A. Mo, M. M'Hamdi, D. Viano, and C. Davidson: *Metall. Mater. Trans. A*, 2006, vol.
728   37, pp. 705–14.
729   12 A. Stangeland, A. Mo, Ø. Nielsen, M. M'Hamdi, and D. Eskin: *Metall. Mater. Trans. A*, 2004, vol.
730   35, pp. 2903–15.
731   13 L. Katgerman: *JOM*, 1982, vol. 34, pp. 46–9.
732   14 M. Lalpoor: Ph.D. Thesis, Delft University of Technology (TU Delft), The Netherlands, 2010.
733   15 M. Lalpoor, D.G. Eskin, and L. Katgerman: *Int. J. Mater. Res.*, 2011, vol. 102, pp. 1286–93.
734   16 Suyitno, D.G. Eskin, and L. Katgerman: *Key Eng. Mater.*, 2006, vol. 306–308, pp. 977–82.
735   17 A. Stangeland, A. Mo, and D. Eskin: *Metall. Mater. Trans. A*, 2006, vol. 37, pp. 2219–29.
736   18 T.A.S. Subroto: Ph.D. Thesis, Delft University of Technology (TU Delft), The Netherlands, 2014.
737   19 D.G. Eskin, V.I. Savran, and L. Katgerman: *Metall. Mater. Trans. A*, 2005, vol. 36, pp. 1965–76.
738   20 T. Subroto, A. Miroux, D. Mortensen, M. M'Hamdi, D.G. Eskin, and L. Katgerman: *IOP Conf. Ser.:*
739   *Mater. Sci. Eng.*, 2012, vol. 33, p. 012068.
740   21 M. M'Hamdi, A. Mo, and H.G. Fjær: *Metall. Mater. Trans. A*, 2006, vol. 37, pp. 3069–83.
741   22 M. Lalpoor, D.G. Eskin, D. Ruvalcaba, H.G. Fjær, A. Ten Cate, N. Ontijt, and L. Katgerman: *Mater.*
742   *Sci. Eng., A*, 2011, vol. 528, pp. 2831–42.
743   23 M. Lalpoor, D.G. Eskin, and L. Katgerman: *Metall. Mater. Trans. A*, 2009, vol. 40, pp. 3304–13.
744   24 T. Subroto, A. Miroux, D.G. Eskin, and L. Katgerman: *Mater. Sci. Eng., A*, 2017, vol. 679, pp. 28–35.
745   25 D.G. Eskin: *Physical Metallurgy of Direct Chill Casting of Aluminum Alloys*, CRC Press/Taylor &
746   Francis, Boca Raton, FL, USA, 2008.
747   26 E. Giraud, M. Suery, and M. Coret: *Metall. Mater. Trans. A*, 2010, vol. 41, pp. 2257–68.
748   27 W.M. van Haaften, B. Magnin, W.H. Kool, and L. Katgerman: *Metall. Mater. Trans. A*, 2002, vol.
749   33, pp. 1971–80.
750   28 O. Ludwig, J.-M. Drezet, C.L. Martin, and M. Suéry: *Metall. Mater. Trans. A*, 2005, vol. 36, pp.
751   1525–35.
752   29 O. Ludwig, J.-M. Drezet, P. Ménésès, C.L. Martin, and M. Suéry: *Mater. Sci. Eng., A*, 2005, vol.
753   413–414, pp. 174–9.
754   30 D. Fabrègue, A. Deschamps, M. Suéry, and W.J. Poole: *Metall. Mater. Trans. A*, 2006, vol. 37, pp.
755   1459–67.
756   31 O. Ludwig, B. Commet, J.-M. Drezet, C.L. Martin, and M. Suery: in *Proc. MCWASP X, 10th Int. Conf.*
757   *on Modeling of Casting, Welding and Advanced Solidification Processes*, TMS, Warrendale, PA,
758   2003, pp. 183–90.
759   32 O. Ludwig, C.L. Martin, and M. Suéry: *Mater. Forum*, 2004, vol. 28, pp. 357–62.
760   33 C.L. Martin, M. Braccini, and M. Suéry: *Mater. Sci. Eng., A*, 2002, vol. 325, pp. 292–301.
761   34 C. Martin, O. Ludwig, and M. Suéry: in *Proc. WCCM V, World Congr. on Computational Mechanics*
762   *V*, Vienna University of Technology, Vienna, 2002.
763   35 H.G. Fjær and A. Mo: *Metall. Trans. B*, 1990, vol. 21, pp. 1049–61.
764   36 T. Subroto, A. Miroux, D.G. Eskin, K. Ellingsen, A. Marson, M. M'Hamdi, and L. Katgerman: in *Proc.*
765   *ICF13, 13th International Conf. on Fracture*, Beijing, China, 2013, pp. 2528–36.
766   37 T.A.S. Subroto, A.G. Miroux, D.G. Eskin, and L. Katgerman: *IOP Conf. Ser.: Mater. Sci. Eng.*, 2011,
767   vol. 27, p. 012074.
768   38 A. Alankar and M.A. Wells: *Mater. Sci. Eng., A*, 2010, vol. 527, pp. 7812–20.
769   39 A.B. Phillion, S. Thompson, S.L. Cockcroft, and M.A. Wells: *Mater. Sci. Eng., A*, 2008, vol. 497, pp.
770   388–94.
771   40 G. Chen, F. Lin, S. Yao, F. Han, B. Wei, and Y. Zhang: *J. Alloys Compd.*, 2016, vol. 674, pp. 26–36.
772   41 L. Sweet, M.A. Easton, J.A. Taylor, J.F. Grandfield, C.J. Davidson, L. Lu, M.J. Couper, and D.H.
773   Stjohn: *Metall. Mater. Trans. A*, 2013, vol. 44, pp. 5396–407.
774   42 V. Mathier, P.-D. Grasso, and M. Rappaz: *Metall. Mater. Trans. A*, 2008, vol. 39, pp. 1399–409.

775   43 I. Farup, J.-M. Drezet, and M. Rappaz: *Acta Mater.*, 2001, vol. 49, pp. 1261–9.
776   44 M. Rappaz, J.-M. Drezet, P.-D. Grasso, and A. Jacot: in *Proc. MCWASP X, 10th Int. Conf. on*
777   *Modeling of Casting, Welding and Advanced Solidification Processes*, TMS, Warrendale, PA, 2003,
778   pp. 53–60.
779   45 Y. Takayama, T. Tozawa, and H. Kato: *Acta Mater.*, 1999, vol. 47, pp. 1263–70.
780   46 D.C. Weckman and P. Niessen: *Metall. Trans. B*, 1982, vol. 13, pp. 593–602.
781   47 M. Rappaz, J.-M. Drezet, and M. Gremaud: *Metall. Mater. Trans. A*, 1999, vol. 30, pp. 449–55.
782   48 S. Mihanyar, A. Mo, M. M'Hamdi, and K. Ellingsen: *Metall. Mater. Trans. A*, 2011, vol. 42, pp.
783   1887–95.
784   49 J.A. Spittle and A.A. Cushway: *Met. Technol.*, 1983, vol. 10, pp. 6–13.
785   50 J. Campbell and T.W. Clyne: *Cast Met.*, 1990, vol. 3, pp. 224–6.
786   51 D.G. Eskin, L. Katgerman, Suyitno, and J.F. Mooney: *Metall. Mater. Trans. A*, 2004, vol. 35, pp.
787   1325–35.
788   52 D. Eskine, J. Zuidema, and L. Katgerman: *Int. J. Cast Met. Res.*, 2002, vol. 14, pp. 217–23.
789   53 L. Zhang, D.G. Eskin, M. Lalpoor, and L. Katgerman: *Mater. Sci. Eng., A,* 2010, vol. 527, pp. 3264–
790   70.
791   54 B. Magnin, L. Maenner, L. Katgerman, and S. Engler: *Mater. Sci. Forum*, 1996, vol. 217–222, pp.
792   1209–14.
793